Turbulence spectra characteristics of high order schemes for direct and large eddy simulation

Foluso Ladeinde [a,*], Xiaodan Cai [a], Miguel R. Visbal [b], Datta V. Gaitonde [b]

[a] *Aerospace Research Corp., L.I., P.O. Box 1527, Stony Brook, Long Island, NY 11790, USA*
[b] *Air Vehicles Directorate, Air Force Research Laboratory, Wright-Patterson AFB, OH 45433, USA*

Abstract

The comparative resolution of the high wavenumber portion of compressible turbulence energy spectrum by some high order numerical schemes is presented in this paper. Included in this are the essentially nonoscillatory (ENO) schemes, the weighted essentially nonoscillatory schemes (WENO), and the compact differencing schemes. The governing equations are the Navier–Stokes equations and the objective is to identify the numerical scheme that best represents the physics of compressible turbulence. Mach numbers M_1 values of 0.1, 0.5 and 0.7 are studied. The compact differencing schemes need filters for numerical stability. It is found in this work that a parameter in the filter scheme provides some flexibility for controlling the physical turbulence energy transfer rate at high wavenumbers, vis-à-vis the numerical dissipation at those scales. Although the ENO schemes do not require filters for numerical stability, the present study shows that the addition of filters improves the energy transfer process at high wavenumbers. Without filtering, with relatively coarse grids, numerical turbulence caused by stencil adaptation persists. This limits the useful wavenumber resolution range of the ENO schemes. The WENO schemes do not require the stabilizing filters but the results tend to be slightly more dissipative. Finally, at low Mach numbers, the current compact differencing and filter scheme formulation gives better results but as the Mach number increases the relative suitability of the ENO method increases. © 2001 IMACS. Published by Elsevier Science B.V. All rights reserved.

Keywords: Turbulence spectra; Essentially nonoscillatory schemes; Compact schemes; High-order schemes; Filters; Direct numerical simulation; Large eddy simulation

1. Introduction

This paper continues the search for the "best" high order numerical method for the direct numerical simulation (DNS) and large eddy simulation (LES) of compressible turbulence. Two promising candidates are the compact and essentially nonoscillatory (ENO) schemes, or combinations thereof. Although many quantities are calculated and presented, the main focus of this paper is on the differential

---

representation of the spectral distribution of turbulence energy by the various schemes. This quantity is of tremendous importance in theoretical turbulence and most of the current understanding of turbulence energy cascade are based on it. This paper compares the ability of the compact schemes, the ENO schemes, the weighted ENO (WENO) schemes, and the pseudospectral schemes to represent the decay of turbulence spectral energy. Included in the present study are the effects of the compact filters and filter parameters on the compact differencing results, as well as the commutativity of filtering and compact differencing. This paper also extends the standard ENO scheme by combining it with compact filters in an attempt to improve the ENO results at the high wavenumber end of the turbulence energy spectrum.

The vehicle used for the study is the decaying homogeneous turbulence problem of Ghosh and Matthaeus [7], hereafter referred to as GM, who employed the pseudospectral method. The first direct numerical simulation of two-dimensional isotropic compressible turbulence was reported by Passot and Pouqet [15]. The GM problem was chosen because of the thorough theoretical treatment. The problem is also two-dimensional which, compared to its three-dimensional counterpart, makes it more affordable and hence more suitable for the kind of parametric study undertaken in this paper. Note that the computational cost associated with the parametric nature of the present studies precludes meaningful three-dimensional turbulence calculations. The consequence of using a two-dimensional model instead of three might not be that serious. From spectral energy standpoint, the differences between two-dimensional and three-dimensional turbulence are explainable in terms of *aliasing*. This phenomenon occurs at the larger scales (small wave numbers) of flow. On the other hand, the focus of the present paper is on the behavior at the high wave numbers, where the turbulence is isotropic and independent of the dimensionality of the flow. Therefore, a two-dimensional model appears suitable and the basic results are not expected to be different in three dimensions. Note that the reference pseudospectral results were generated in Ref. [7]. Although the geometry in GM is rectangular, the formulation for both the ENO and compact schemes assumes a complex geometry and hence uses a curvilinear coordinate transformation. The unsteady, two-dimensional, viscous Navier–Stokes equations are solved in strong conservation form using the generalized curvilinear coordinates (ξ, η):

$$\frac{\partial}{\partial t}\left(\frac{U}{J}\right) + \frac{\partial F}{\partial \xi} + \frac{\partial G}{\partial \eta} = \frac{1}{Re}\left[\frac{\partial F_v}{\partial \xi} + \frac{\partial G_v}{\partial \eta}\right], \tag{1}$$

where $U = \{\rho, \rho u, \rho v, \rho E_t\}$ is the solution vector, J is the Jacobian of the transformation, F, G are the inviscid fluxes and F_v, G_v are the viscous fluxes.

The initial condition for this problem is of the pseudosound type and is obtained by first solving for the fluctuating pressure p' from the Poisson equation for the incompressible component of the initial velocity field:

$$\nabla^2 p' = -\gamma M_1^2 \nabla(\boldsymbol{u}^I \cdot \nabla \boldsymbol{u}^I),$$

where the right-hand side of this equation is due solely to the solenoidal velocity component $\boldsymbol{u}^I$ from random numbers. The pseudosound density fluctuation is obtained from the relation $\delta\rho_{\text{PS}} = (1/\gamma)p'$ and the initial pressure and density fields are $P = 1 + p'$ and $\rho = 1 + \delta\rho_{\text{PS}}$. The imposed turbulence spectrum is chosen to match that in GM:

$$E_i = \begin{cases} 1, & 1 \leqslant k \leqslant \sqrt{12}, \\ 0, & \text{otherwise}, \end{cases}$$

where "i" is an index defined by $i - \frac{1}{2} \leqslant k \leqslant i + \frac{1}{2}$, with $k = \sqrt{k_x^2 + k_y^2}$ and k_x, k_y are the turbulence wavenumbers in the x- and y-directions, respectively. The Mach number is $M_1 = 0.5$ and the Reynolds

number is 250. As in GM, a grid of 64^2 is sufficient to resolve all scales of flow. The computational length of the domain runs from 0.0 to 7.081 units in both x and y (and as noted above, although the grid is uniform, a full curvilinear coordinate transformation is used). Results for 256^2 are also analyzed for grid dependence. The gas is assumed to be polytropic, with $P = \rho^\gamma$ and T (temperature) $= \rho^{\gamma-1} \gamma M_1^2$. Note that the total energy equation is solved, nevertheless.

2. Compact differencing

In the framework of compact differencing, the derivative u' for any generic variable u in the transformed coordinate frame is represented as [6,13,23]:

$$\alpha u'_{i-1} + u'_i + \alpha u'_{i+1} = b \frac{u_{i+2} - u_{i-2}}{4\Delta\xi} + a \frac{u_{i+1} - u_{i-1}}{2\Delta\xi}, \tag{2}$$

where α, a, and b are constants which determine the spatial properties of the algorithm. The base compact differencing schemes used in this paper are the three-point, fourth order scheme C4 with $(\alpha, a, b) = (\frac{1}{4}, \frac{3}{2}, 0)$, the five-point, sixth order scheme C6 with $(\alpha, a, b) = (\frac{1}{3}, \frac{14}{9}, \frac{1}{9})$. Also used is the five-point, fourth order scheme O5 with $(\alpha, a, b) = (0.430816, 1.6205440, 0.2410880)$. This scheme minimizes the dispersion error over the entire range of wavenumbers up to 2 points per wave. Note that the symbol u above also represents vector quantities such as the U vector defined in Eq. (1).

Eq. (2) is used to calculate the various derivatives in the (ξ, η) plane, as well as the metrics from coordinate transformation. The inviscid fluxes in the Navier–Stokes equations are formed in the transformed coordinates at each nodal point and the components differentiated using Eq. (2). The same coefficients (α, a, b) are used for both the metrics and the fluxes, which is useful in reducing the error on stretched meshes [5,22]. To calculate the viscous and heat conduction terms, the primitive variables $u = \{\rho, \rho u, \rho v, \rho E_t\}$ are first compact differentiated to form the stress tensor and heat flux vector. The viscous and heat conduction terms of the flow equations are then computed by another application of Eq. (2). The use of second derivative compact formulations, as in Ref. [13], has some advantages but could lead to excessive computational penalty on curvilinear coordinates.

The compact formulas for the domain boundary points are well known; the present work is based on the boundary formulas in Refs. [6,23]. Time integration of the ODE that results from the spatial integration was based on the classical fourth order Runge–Kutta scheme [4].

2.1. Spatial filtering

Numerical instability is often encountered in the solution of the Navier–Stokes equations with compact differencing. The sources of instability include boundary condition implementation, unresolved scales, mesh non-uniformities, and the nonlinearity of the flow equations. Spurious waves amplify and destroy the solution if left unchecked. Artificial dissipation, wherein a small additive damping term is explicitly added to the governing equations, is a popular method for suppressing the instabilities. However, this method is undesirable for calculations intended to examine the physics of the flow, such as direct numerical simulation (DNS) or large-eddy simulation (LES) of turbulence. The newly rediscovered alternative method of filtering is of interest in this paper because of recent development of high order

filters that match the high order compact differencing of the flow equations. In the formulation, the filtered values $\widetilde{u}$ for any quantity u in the transformed plane is represented as [6,13,23]:

$$\alpha_f \widetilde{u}_{i-1} + \widetilde{u}_i + \alpha_f \widetilde{u}_{i+1} = \sum_{n=0}^{N} \frac{a_n}{2}(u_{i+n} + u_{i-n}). \tag{3}$$

This representation provides a non-dispersive, $2N$th-order filter with $2N + 1$ point stencil. The spectral function F for this scheme can be represented as

$$F(\omega) = \frac{\sum_{n=0}^{N} a_n \cos(n\omega)}{1 + 2\alpha_f \cos(\omega)},$$

where ω is the normalized wavenumber $\omega = 2\pi k/N$, $N = L/h$, k is the physical wavenumber, L is domain length and h is the grid spacing. The eighth and tenth order filters are used in the present work, for which the coefficients are:

$$\begin{aligned}
a_0 &= \left(\frac{93+70\alpha_f}{128}, \frac{193+126\alpha_f}{256}\right), & a_1 &= \left(\frac{7+18\alpha_f}{16}, \frac{105+302\alpha_f}{256}\right), \\
a_2 &= \left(\frac{-7+14\alpha_f}{32}, \frac{15(-1+2\alpha_f)}{64}\right), & a_3 &= \left(\frac{1}{16} - \frac{\alpha_f}{8}, \frac{45(1-2\alpha_f)}{512}\right), \\
a_4 &= \left(-\frac{1}{128} + \frac{\alpha_f}{64}, \frac{5(1-2\alpha_f)}{512}\right), & a_5 &= \left(0, \frac{1-2\alpha_f}{512}\right).
\end{aligned} \tag{4}$$

The foregoing filters are a subset of the more elaborate ones proposed by Gaitonde and Visbal [6]. For the convenience of reference, we will refer to their filters as VG filters. The boundary treatments in VG filters are available in the reference.

2.2. Commutativity of filtering and compact differencing

It is interesting to explore the commutativity of the filtering and compact differencing operations. To this end, the filter scheme can be written in a matrix form as

$$F\widetilde{\Phi} = M\Phi$$

and the compact differencing scheme as

$$P\Phi' = N\Phi.$$

Pre-filtering, i.e., filtering before compact differencing produces

$$(\widetilde{\Phi})' = P^{-1}N\widetilde{\Phi} = (P^{-1}N)(F^{-1}M)\Phi = AB\Phi,$$

whereas, post-filtering, i.e., compact differencing before filtering gives

$$\widetilde{(\Phi')} = (F^{-1}M)(P^{-1}N)\Phi = BA\Phi,$$

where $\Phi, \widetilde{\Phi}, \Phi', \widetilde{(\Phi')}$, and $(\widetilde{\Phi})'$ are $n \times 1$ vectors and F, M, P, N are $n \times n$ matrices. In general, $AB \neq BA$, and the two operations do not commute. However, for the special case of periodic boundary conditions, A and B are symmetric and pre-filtering and post-filtering produce identical results. We have confirmed this result in the numerical calculations of known functions, as shown later with periodic and Dirichlet boundary conditions.

3. ENO and WENO schemes

ENO schemes were first developed in Refs. [8,9]. Shu and Osher [19,20] simplified the original procedure, while Refs. [1–3,11,12,21] have applied Shu's version of ENO to simulate compressible turbulence. The WENO schemes are more recent and are attributable to the work of Liu et al. [14] and Jiang and Shu [10]. An excellent review article on ENO and WENO is available in Shu [18].

For the present paper, the ENO/WENO procedure pertains to the differencing of the convective terms of the Navier–Stokes equations in a way that avoids discretization across very strong gradients. (The viscous terms are discretized with fourth order central schemes.) Thus, based on the Navier–Stokes equations in (1), the ENO problem can be written as

$$u_t(\xi, \eta, t) + f_\xi(u(\xi, \eta, t)) + g_\eta(u(\xi, \eta, t)) = 0, \tag{5}$$

where it is apparent that u, f, and g are vector functions. The convective terms are reconstructed to accuracy k, which is taken as 3 or 4 in the present work. The basic ENO differencing problem is

$$\frac{\mathrm{d}u_{ij}}{\mathrm{d}t} = -\frac{1}{\Delta\xi}(\widehat{f}_{i+1/2,j} - \widehat{f}_{i-1/2,j}) - \frac{1}{\Delta\eta}(\widehat{g}_{i,j+1/2} - \widehat{g}_{i,j-1/2}) = f' + g' + \mathrm{O}(\Delta\xi^k, \Delta\eta^k)$$
$$\equiv L(u). \tag{6}$$

The method of lines is used, so the time derivative is suppressed in the following development. The specific ENO/WENO procedure used in this work will be illustrated with the calculation of $\widehat{f}_{i+1/2,j}$, and sufficient details will be given to allow the reproduction of the results in this paper. Many options are possible with the ENO or WENO schemes, as the paper by Shu [18] summarizes. The base ENO scheme in the present paper, which uses the procedure by Shu, focuses on the characteristic-wise high order finite differencing with Roe speed and Lax–Friedrichs flux-splitting. The specific approach is now summarized:

1. The divided (or undivided differences) of $f(u)$ and u are computed for all i in the grid, with j frozen.
2. At each fixed $\xi_{i+1/2,j}$, we:
   (i) Compute the average state $u_{i+1/2,j}$ using a Roe average satisfying the mean value theorem.
   (ii) Compute the right and left eigenvectors, the eigenvalues of the Jacobian $\partial f/\partial u$ evaluated at $(i + \frac{1}{2}, j)$. Denote the eigenvectors by

   $$R = R(u_{i+1/2,j}), \qquad R^{-1} = R^{-1}(u_{i+1/2,j}),$$

   respectively.
   (iii) Determine the potential stencil for the ENO and WENO reconstruction of $\widehat{f}_{i+1/2,j}$ using the value of k, the current point $(i + \frac{1}{2}, j)$ and the specification of a "preferred" or one-point upwind stencil.
   (iv) Transform those differences computed in step 1 above which are contained in the potential stencil using the modal matrices:

   $$v_m = R^{-1}u_m, \qquad h_m = R^{-1}f(u_m)$$

   for m in a neighborhood of i.

(v) For each component of the characteristic variables, obtain the corresponding component of the characteristic numerical flux $h_{i+1/2,j}^{\pm}$ as follows:

- Split the flux h:

$$h(v) = h^+(v) + h^-(v).$$

With Roe speeds and Lax–Friedrichs splitting, this procedure makes available the values $h^+(v_i)$ and $h^-(v_i)$, which can be considered as cell centroid or cell average values $(\overline{h})^+(v_i)$ and $(\overline{h})^-(v_i)$ in relation to the cell boundary.

- Starting from the two-point stencil

$$S(i) = \{\xi_i\}$$

and adding points to the stencil in the ENO fashion (i.e., by comparing divided or undivided differences), we compute high order cell boundary values as

$$\widehat{h}_{i+1/2,j}^+ \equiv \left(h_{i+1/2,j}^+\right)^- = \sum_{m=0}^{k-1} c_{rm}(\overline{h})^+_{\,i-r+m},$$

$$\widehat{h}_{i+1/2,j}^- \equiv \left(h_{i+1/2,j}^-\right)^+ = \sum_{m=0}^{k-1} \widetilde{c}_{rm}(\overline{h})^-_{\,i-r+m+1},$$

where c_{rm} is the Lagrange interpolation:

$$c_{rm} = \left(\sum_{p=m+1}^{k} \frac{\sum_{l=0,l\neq p}^{k} \prod_{q=0,q\neq p,l}^{k}(\xi_{i+1/2} - \xi_{i-r+q-1/2})}{\prod_{l=0,l\neq p}^{k}(\xi_{i-r+p-1/2} - \xi_{i-r+l-1/2})} \right) \Delta\xi_{i-r+m}.$$

Thus, the reconstructed fluxes, in characteristic space, at $\xi_{i+1/2}$ are $\widehat{h}_{i+1/2,j}^-$ and $\widehat{h}_{i+1/2,j}^+$.

- $\widehat{h}_{i+1/2,j}^-$ and $\widehat{h}_{i+1/2,j}^+$ are transformed back to the physical space using

$$\widehat{f}_{i+1/2}^{\pm} = R\widehat{h}_{i+1/2,j}^{\pm}.$$

The boundary flux $\widehat{f}_{i-1/2}^{\pm}$ is obtained in a similar fashion, as are the η derivatives $\widehat{g}_{i+1/2}^{\pm}$ and $\widehat{g}_{i-1/2}^{\pm}$. Hence, Eq. (6) becomes an ODE for the calculation of $u_{ij}(t)$, for which we used procedures in Refs. [19,20].

- For WENO, one uses a convex combination of all the candidate stencils, instead of using just one of these. If

$$S_r(i) = \{\xi_{i-r}, \ldots, \xi_{i-r+k-1}\}, \quad r = 0, \ldots, k-1,$$

denotes the rth stencil, the value $h_{i+1/2,j}^{(r)}$ would be calculated from formulas of the form

$$\widehat{h}_{i+1/2,j}^+ \equiv \left(h_{i+1/2,j}^+\right)^- = \sum_{r=0}^{k-1} \omega_r \sum_{m=0}^{k-1} c_{rm}(\overline{h})^+_{\,i-r+m},$$

$$\widehat{h}_{i+1/2,j}^- \equiv \left(h_{i+1/2,j}^-\right)^+ = \sum_{r=0}^{k-1} \widetilde{\omega}_r \sum_{m=0}^{k-1} \widetilde{c}_{rm}(\overline{h})^-_{\,i-r+m+1}.$$

The determination of the weights ω_r and $\widetilde{\omega}_r$ is described in detail elsewhere [10,18]. Note that for WENO,

$$h_{i+1/2,j} = h(\xi_{i+1/2,j}) + O(\Delta\xi^{2k-1}),$$

meaning that WENO is theoretically more accurate than ENO ($2k - 1$ versus k) for the same stencil size.

3.1. Filtered ENO

Unlike the compact scheme solution of the Navier–Stokes equations where the use of filters is usually indicated for stability, ENO calculations are stable without filters. However, our investigation of the high wavenumber end of ENO-generated turbulence spectrum has shown that the spectral energy (both kinetic and internal) does not go to zero the way it should, based on homogeneous turbulence theory. Thus, there is a residual energy at the high wavenumbers which appears to be due to the numerics. The adaptive stencil in ENO causes some high wavenumber oscillations which manifest as turbulence fluctuations. As shown later in this paper, this numerical turbulence is absent in the filtered compact differencing scheme results for the Navier–Stokes simulations as well as in the WENO results at comparable grid resolution. It is also absent in the ENO results in very fine grid resolutions. To remedy this problem with the standard ENO scheme, we have extended the ENO method to use a subset of the compact-based VG filters. The formulation follows that presented earlier except that the filters are applied to the computed ENO results at a predetermined frequency during the time stepping of the solution. Thus, Eq. (3) is applied with the quantity u being the ENO result and $\tilde{u}$, its corresponding filtered value. The previous discussions on the spectral function $F(\omega)$ and the free parameter α_f also hold.

4. Turbulence spectra

The objective of the present study is to compare the turbulence spectra from different high order schemes. Although a semi-analytical method for assessing the spectral response of finite-difference schemes is proposed in Ref. [13], the relevance to turbulence simulation and modeling was not included in the study; neither was the implementation of, and the comparison with, the ENO or WENO schemes. In the present study turbulence spectra are presented for both the kinetic energy E_k and internal energy E_i and are discretized as follows:

$$E_k = \frac{1}{2} \sum_{k=1}^{N/2} p^k(k) n(k) \quad \text{and} \quad E_i = \sum_{k=1}^{N/2} p^i(k) n(k),$$

where N is the number of grid points and $n(k)$ is the number of Fourier modes in the kth integer bin and satisfies

$$n(k) = \sum_{k_1} \sum_{k_2}^{k-1/2 \leqslant \sqrt{k_1^2 + k_2^2} < k+1/2} 1.$$

The functions $p^k(k)$, $p^i(k)$ are the spectra for the kinetic and internal energy components, respectively, with the definition

$$p^k(k) = \sum_{k_1} \sum_{k_2}^{k-1/2 \leqslant \sqrt{k_1^2 + k_2^2} < k+1/2} \left(\widehat{u}_1^2(k_1, k_2) + \widehat{u}_2^2(k_1, k_2) \right) / n(k),$$

$$\widehat{u}_1(k_1, k_2) = \frac{1}{N_1 N_2} \sum_{j=1}^{N_2} \sum_{i=1}^{N_1} u_1(i, j) \mathrm{e}^{-\widehat{\mathrm{i}}2\pi k_1 i/N_1} \mathrm{e}^{-\widehat{\mathrm{i}}2\pi k_2 j/N_2},$$

$$\widehat{u}_2(k_1, k_2) = \frac{1}{N_1 N_2} \sum_{j=1}^{N_2} \sum_{i=1}^{N_1} u_2(i, j) \mathrm{e}^{-\widehat{\mathrm{i}}2\pi k_1 i/N_1} \mathrm{e}^{-\widehat{\mathrm{i}}2\pi k_2 j/N_2}.$$

The expression for $p^i(k)$ is similar, using the definition provided below for E_{int}. Other spectrum-related quantities include the longitudinal velocity component (U^{L}), the transverse velocity component (U^{T}), and the turbulent velocity (U^{Turb}), which can be discretized as

$$U^{\mathrm{L}} = \langle (u_1^{\mathrm{L}})^2 + (u_2^{\mathrm{L}})^2 \rangle^{1/2},$$
$$U^{\mathrm{T}} = \langle (u_1^{\mathrm{T}})^2 + (u_2^{\mathrm{T}})^2 \rangle^{1/2}$$

and

$$U^{\mathrm{Turb}} = \langle (u_1^{\mathrm{Turb}})^2 + (u_2^{\mathrm{Turb}})^2 \rangle^{1/2},$$

where

$$\boldsymbol{u}^{\mathrm{L}}(i, j) = \sum_{k_1=-N_1/2}^{N_1/2-1} \sum_{k_2=-N_2/2}^{N_2/2-1} \boldsymbol{k} \frac{k_1 \widehat{u}_1(k_1, k_2) + k_2 \widehat{u}_2(k_1, k_2)}{(k_1^2 + k_2^2)} \mathrm{e}^{\widehat{\mathrm{i}}2\pi k_1 i/N_1} \mathrm{e}^{\widehat{\mathrm{i}}2\pi k_2 j/N_2},$$

$$\boldsymbol{u}^{\mathrm{T}}(i, j) = \sum_{k_1=-N_1/2}^{N_1/2-1} \sum_{k_2=-N_2/2}^{N_2/2-1} \left(\widehat{\boldsymbol{u}}(k_1, k_2) - \boldsymbol{k} \frac{k_1 \widehat{u}_1(k_1, k_2) + k_2 \widehat{u}_2(k_1, k_2)}{(k_1^2 + k_2^2)} \right) \mathrm{e}^{\widehat{\mathrm{i}}2\pi k_1 i/N_1} \mathrm{e}^{\widehat{\mathrm{i}}2\pi k_2 j/N_2},$$

$$\boldsymbol{u}^{\mathrm{Turb}}(i, j) = \sum_{k_1}^{\sqrt{k_1^2+k_2^2}>1.0} \sum_{k_2} \left(\widehat{\boldsymbol{u}}(k_1, k_2) - \boldsymbol{k} \frac{k_1 \widehat{u}_1(k_1, k_2) + k_2 \widehat{u}_2(k_1, k_2)}{(k_1^2 + k_2^2)} \right) \mathrm{e}^{\widehat{\mathrm{i}}2\pi k_1 i/N_1} \mathrm{e}^{\widehat{\mathrm{i}}2\pi k_2 j/N_2}.$$

The total kinetic E_{k} and internal energy E_{int} are global quantities and can be defined as

$$E_{\mathrm{k}} = \frac{1}{2} \sum_{i=1}^{N_1} \sum_{j=1}^{N_2} (\rho u_1^2(i, j) + \rho u_2^2(i, j))/(N_1 N_2) = \frac{1}{2} \langle u_1^2 + u_2^2 \rangle,$$

$$E_{\mathrm{int}} = \frac{\langle \rho^\gamma \rangle - \langle \rho \rangle^\gamma}{M_1^2 \gamma (\gamma - 1)}.$$

5. Overall computational sequence

The sequence of the calculations for the Navier–Stokes problem can be summarized as follows:
1. Specify Mach number M_1, Reynolds number Re, and generate the turbulent pseudosound initial conditions

$$u_0 = (\rho_0, (\rho u)_0, (\rho v)_0, E_0),$$

by solving the Poisson equation.
2. Load the initial condition into the executable code for ENO, WENO, or the compact differencing code.

3. Start the time loop. At each time step n carry out the following calculations:
   (i) Determine the CFL for the time step.
   (ii) Compute $L(u^n)$ in Eq. (6) using ENO, WENO, or the compact code.
   (iii) Solve the ODE problem in Eq. (6) using the third order, TVD Runge–Kutta procedure in Refs. [19,20] for ENO/WENO, and a standard fourth order, multi-step Runge–Kutta procedure [4] for the compact code.
   (iv) Calculate the filtered solution $\widetilde{u}^n$, if compact differencing or filtered ENO scheme.
   (v) Compute $M_s^2(t^n)$, $E_k(t^n)$, $E_{int}(t^n)$ and $U^T(t^n)/U^L(t^n)$.
   (vi) Compute $P_{kin}(\kappa)$ and $P_{int}(\kappa)$ at desired values on the time step n.
   (vii) Test turbulence energy for laminarization. Terminate execution if flow becomes laminar or repeat steps (i)–(vi) otherwise.

6. Results

6.1. Comparison of the basic high order schemes

To help isolate possible complications by the computational environments of the complete flow and energy equations, such as upwinding, filtering, the effects of the viscous terms, and the procedure for their discretization, the basic compact and ENO schemes were first used to calculate the derivatives of two known functions of different derivative steepness. The error and resolution of moderately steep, but continuous, gradients were calculated on several Unix workstations. This provides performance data for the very basic forms of the two schemes and allows the evaluation of the effects of the various capabilities and programming style differences contained in the codes finally used. The full DNS equations for compressible flows, from subsonic to transonic Mach numbers Ma will follow. The latter is based on decaying homogeneous turbulence with pseudosound initial conditions and known initial turbulence energy spectrum.

The functions for the basic tests are:

$$f_1 = \sin(x) \quad (0 \leqslant x \leqslant L_1),$$

$$f_3 = \frac{1}{2}\left(\tanh\left(\frac{x}{a}\right) - \tanh\left(\frac{x - 0.1}{a}\right) \right), \quad a = 0.02 \quad (0 \leqslant x \leqslant L_2).$$

Obviously, f_1 is a much smoother function than f_2 (see Fig. 1). Periodic boundary conditions were used for f_1, so that the interior accuracy was retained at the boundaries for both schemes. Dirichlet end conditions $((f_1)_0 = (f_1)_L = 1)$ were also used in order to demonstrate the commutativity of compact differencing and filtering. Periodic conditions were used at the two end points for f_2. Domain lengths are $(L_1, L_2) = (5.5, 10.0)$.

The notations used in Ref. [6] will be adopted to simplify the specification of the compact difference schemes. When periodic conditions are employed, the notation Cn will be used to denote an nth order compact differencing scheme. When the specification of boundary treatment is important, the precise scheme will be denoted with 5 numbers, a, b, c, d, e, where $a, \ldots, e$ are numbers denoting the order of accuracy of the formulas employed respectively at points 1, 2, $\{3, \ldots, \text{IL} - 2\}$, $\text{IL} - 1$ and IL, where IL is the number of nodal points. For example, 24642 consists of a sixth-order interior compact formula, which degrades to 4th- and 2nd-order accuracy near the boundary. For the filter scheme, the interior order will
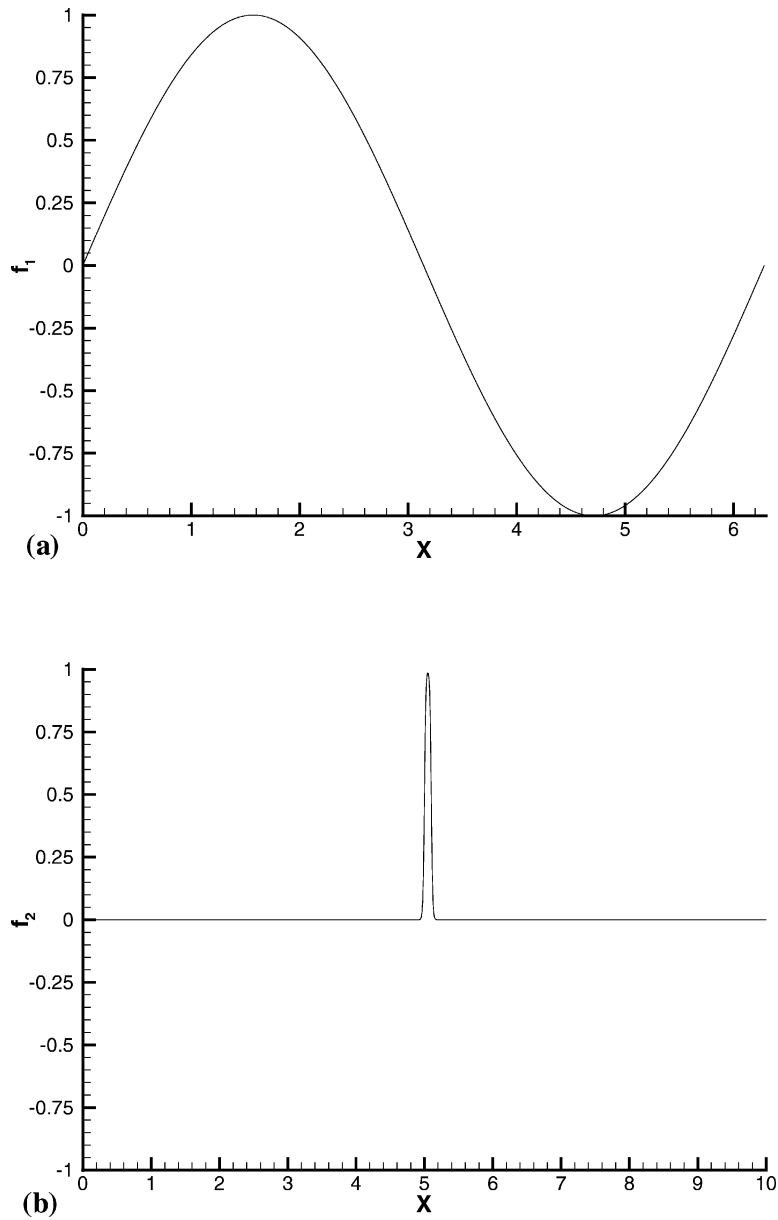
Fig. 1. A sketch of the functions used for the test of the basic compact and ENO algorithms: (a) f_1, (b) f_2.

be designated with its order of accuracy superscripted with the value of a parameter α_f. For example, $F10^{0.3}$ represents a tenth-order filter with $\alpha_f = 0.3$. When boundaries are present, the notation for the boundary filter formulas consists of simply appending the interior filter with the order of accuracy of the formulas at each of the boundary points $1, 2, \ldots$ in sequence. If a point is left unfiltered, the value 0 is utilized. For example, $F10^{0.4}$-0.6.8.8.8 consists of an $\alpha_f = 0.4$ tenth-order interior filter formula which

degrades to 8th-, 8th-, 8th-, and 6th-order accuracy as the boundary is approached from the interior. For this example, the point on the boundary is not filtered.

The basic tests used a third-order treatment for ENO, whereas the compact scheme formula is 24642 along with the filter $F10^{0.3}$-0.2.4.6.8 for both f_1 and f_2. The filter formula $F2^{0.3}$-0.2.2.2.2 was also applied to f_2, for the purpose of investigating filter effects. A kernel code has been written to measure the time costs and numerical accuracy of the above schemes.

Figs. 1–4 are used to illustrate some behavior of the basic schemes. Fig. 2 shows the results for the compact and ENO calculation of $\partial f_1 / \partial x$. For the compact schemes, results are shown for the pre-filtered, post-filtered and the unfiltered cases. Figs. 2(a) and (b) differ in the boundary conditions: Fig. 2(a) uses periodic boundary conditions on $\partial f_1 / \partial x$, whereas Fig. 2(b) uses Dirichlet condition $((f_1)_0 = (f_1)_L = 1)$. A grid of 10 points is sufficient for this problem.

From the figures, all schemes give essentially the same results except that compact differencing and filtering are not commutative for the Dirichlet problem, in agreement with the simple mathematical illustration above. Post-filtering gave results that were closer to the exact. Figs. 3 and 4 show the results for $\partial f_2 / \partial x$ using the same schemes as in Fig. 2. The effects of the filter order for the compact calculation are shown. Fig. 3(a) uses $F10^{0.3}$-0.2.4.6.8 whereas Fig. 3(b) uses $F2^{0.3}$-0.2.2.2.2. Both calculations use 6 grid points in the feature. While both the ENO and compact schemes miscalculate the feature at this grid resolution level, the ENO results are better than the compact results in the sense that the latter exhibits Gibbs-like phenomenon whereas the former does not. The effect of filter order on the compact difference results are not apparent for this problem. Fig. 4 is a high-resolution version of Fig. 3, with 32 grid points in the feature. The results for all schemes are identical at this grid resolution level.

The relative numerical accuracy of the two schemes is dependent on the smoothness of the test function. When the test function is smooth, like f_1, we obtain the numerical results that are consistent with the formal analysis. In this case, the maximum accuracy orders (Table 1) are $O(\Delta \xi^6)$ and $O(\Delta \xi^5)$ for the compact scheme with periodic and Dirichlet boundary conditions, respectively. The maximum accuracy order for ENO (periodic) is $O(\Delta \xi^4)$. The loss of accuracy order when the grid is coarse is believed to be caused by the boundary treatment in the compact scheme. The loss of accuracy order when the grid is fine is caused by the round-off error induced by the computer. Table 1 lists the numerical errors based on the second norm. The compact difference results include both periodic and Dirichlet boundary conditions as well as "pre-filtering" and "post-filtering". Table 2 represents the numerical errors of the two schemes in the smooth regions of f_2'. When the jumps are resolved by using a finer mesh (Fig. 4), the compact scheme restores its higher order resolution capabilities in the whole calculation domain, although the ENO results also show high accuracy.

Note that because f_1 is smooth, filtering when the grid is coarse increases the error via unnecessary dissipation whereas for f_2', which has a strong gradient, the filter helps to dampen out the errors when the grid is coarse, leading to better accuracy than the unfiltered result. Also note that whereas the errors associated with pre-filtering and post-filtering schemes are essentially the same for f_2', they differ for f_1', with post-filtering showing the lower errors. The accuracy results for f_1' in the table are based on the non-periodic case, whereas those for f_2' are based on periodic conditions. Agreement with the simple mathematical illustration provided earlier is evident.
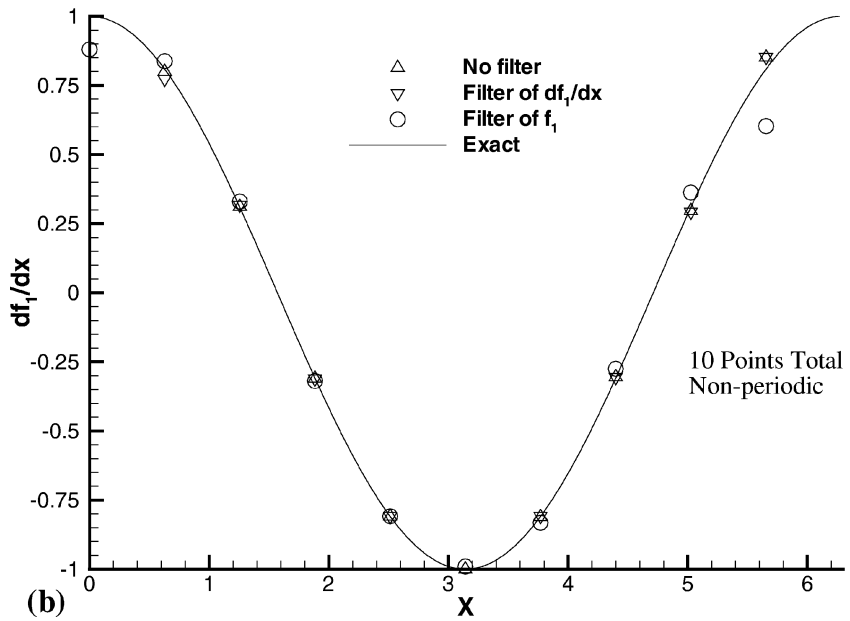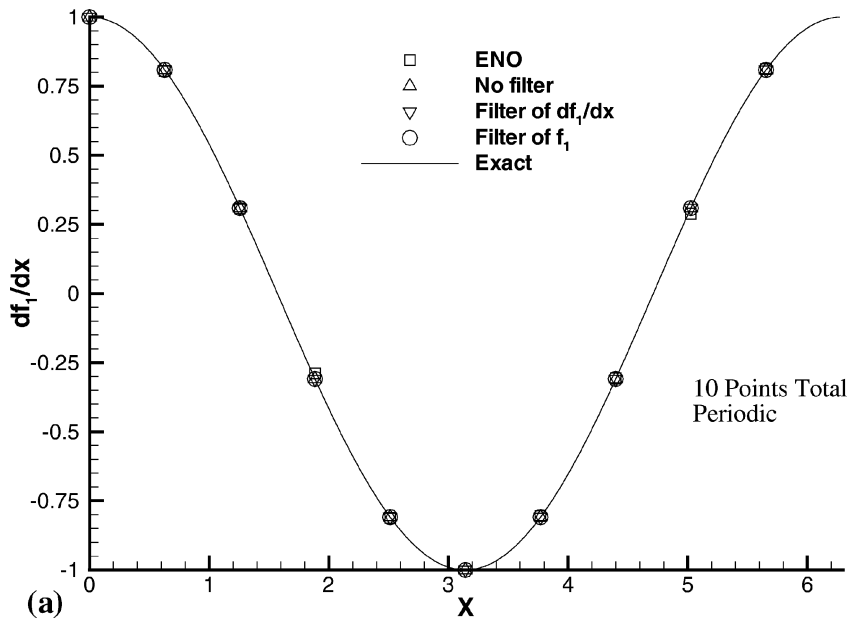
Fig. 2. Comparison of compact and ENO calculation of the derivative of function f_1. (a) Periodic conditions. The compact results include the cases with and without filters. Results for "pre-filtering" and "post-filtering" are shown. (b) Dirichlet conditions. Only compact results are shown in (b) since the purpose of the figure is to illustrate the differential behavior of boundary conditions on the commutativity of the compact differencing and filtering operations.
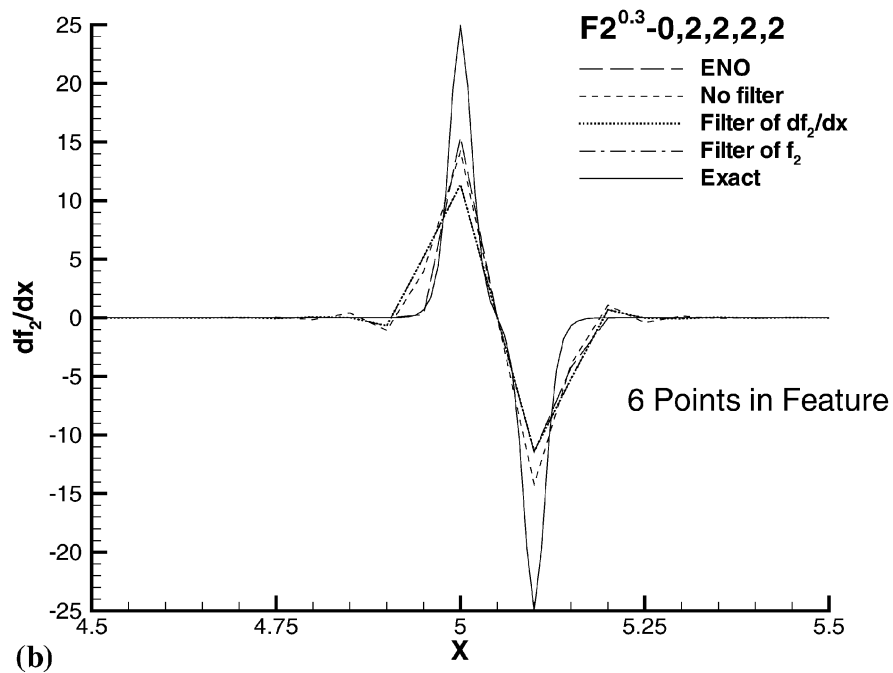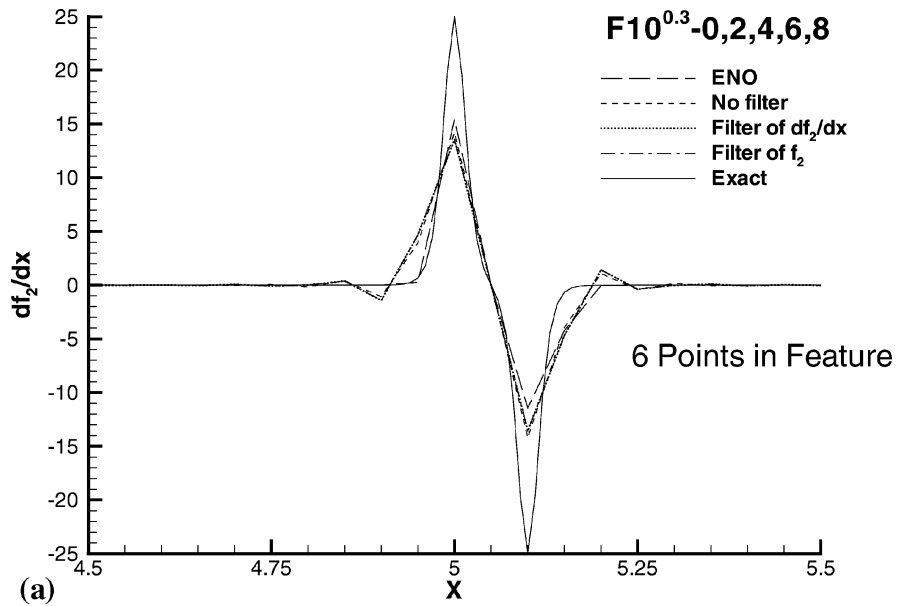
Fig. 3. Comparison of compact and ENO calculation of the derivative of function f_2. The effects of the order of accuracy of the filter is also shown. (a) Tenth-order interior filter. (b) Second-order interior filter. Note that the close-up view in the vicinity of the feature (high gradient region) is shown. The number of nodal points in the feature is 6.
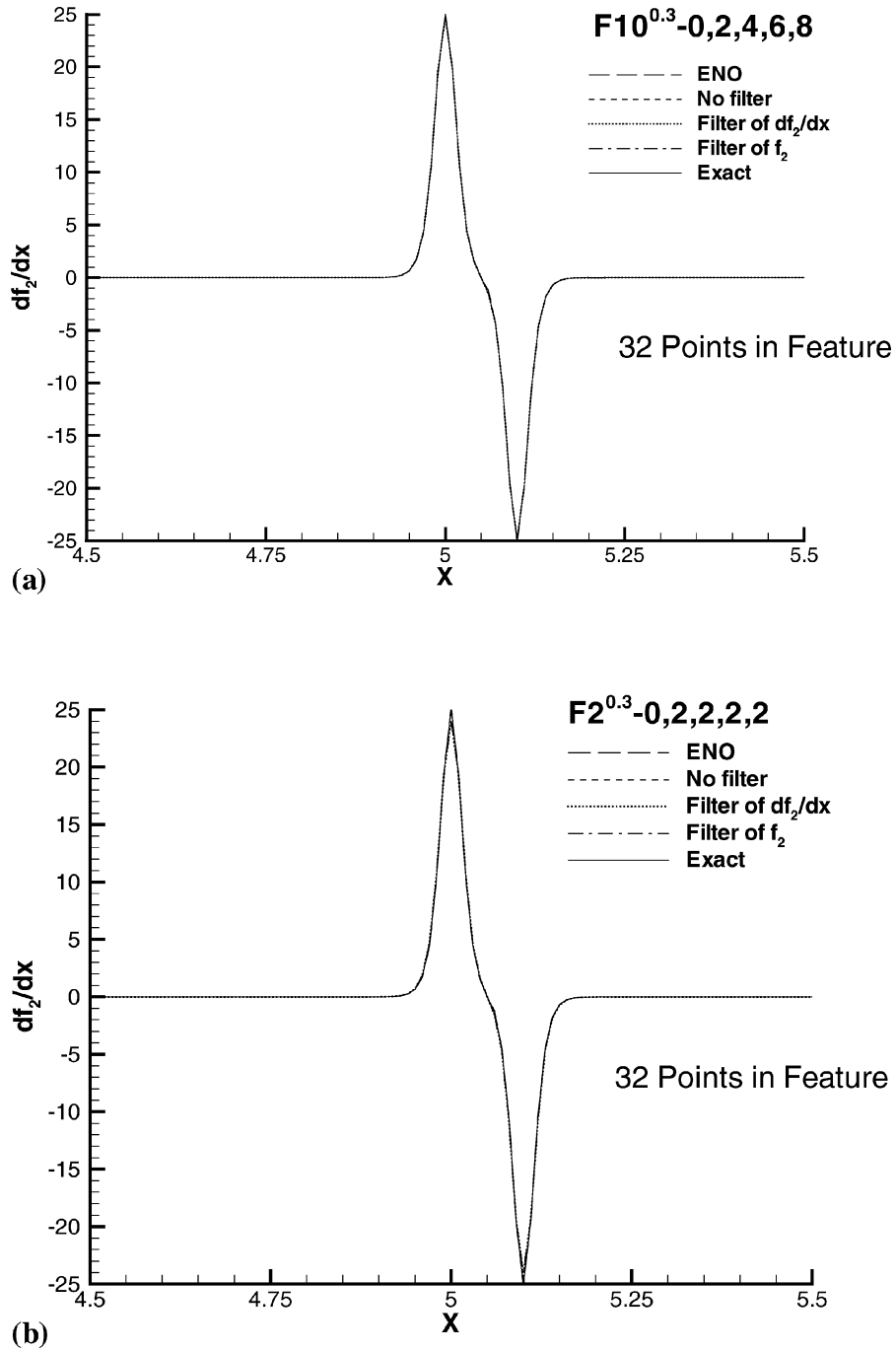
Fig. 4. Comparison of compact and ENO calculation of the derivative of function f_2. The effects of the order of accuracy of the filter is also shown. (a) Tenth-order interior filter. (b) Second-order interior filter. Note that the close-up view in the vicinity of the feature (high gradient region) is shown. The number of nodal points in the feature is 32.

Table 1
Numerical errors in the evaluation of f_1'. "P" and "D" in the table imply "periodic" and "Dirichlet" boundary conditions, respectively

Grid	10	10^2	10^3	10^4	10^5
ENO (P)	9.665×10^{-3}	3.884×10^{-6}	1.307×10^{-9}	5.377×10^{-13}	4.242×10^{-12}
C6, no filter (P)	2.171×10^{-5}	2.073×10^{-11}	2.444×10^{-14}	2.629×10^{-13}	2.915×10^{-12}
C6, pre-filter of f_1(P)	2.322×10^{-5}	2.073×10^{-11}	4.833×10^{-14}	5.203×10^{-13}	5.180×10^{-12}
C6, post-filter of f_1'(P)	2.322×10^{-5}	2.073×10^{-11}	1.624×10^{-14}	2.334×10^{-13}	2.374×10^{-12}
C6, no filter (D)	1.683×10^{-2}	6.909×10^{-7}	2.191×10^{-11}	2.629×10^{-13}	2.915×10^{-12}
C6, pre-filter of f_1(D)	7.931×10^{-2}	4.338×10^{-4}	1.380×10^{-6}	4.363×10^{-9}	1.468×10^{-11}
C6, post-filter of f_1'(D)	2.060×10^{-2}	6.554×10^{-5}	2.081×10^{-7}	6.580×10^{-10}	3.159×10^{-12}

Table 2
Numerical errors in the smooth region of f_2'. Periodic boundary conditions are used

Grid	10	10^2	10^3	10^4	10^5
ENO	4.166×10^{-2}	1.156×10^{-5}	3.567×10^{-3}	1.024×10^{-6}	3.235×10^{-10}
C6, no filter	2.306×10^{-1}	1.466×10^{-1}	8.639×10^{-9}	1.593×10^{-14}	6.004×10^{-14}
C6, pre-filter of f_2	1.763×10^{-1}	1.265×10^{-1}	1.642×10^{-7}	1.605×10^{-14}	4.879×10^{-14}
C6, post-filter of f_2'	1.772×10^{-1}	1.265×10^{-1}	1.642×10^{-7}	1.559×10^{-14}	4.875×10^{-14}

6.2. High order calculation of decaying homogeneous turbulence

Certain characteristics of the decaying turbulence simulation will be pointed out before the results are presented. To simulate isotropic turbulence, the initial conditions were based on random numbers. This implies that the initial conditions would always be different for different levels of grid refinement (for example, 64^2 versus 256^2). This situation is independent of the fact that the random numbers are scalable to desired initial rms values and spectral energy distribution. As a consequence, only certain quantities can be compared between simulations that use different grid resolutions. Obviously, the dependent variables (ρ, ρu, ρv, E, p) cannot be compared. However, the averaged quantities: temporal total kinetic (E_k) and internal energy (E_{int}), temporal rms values, etc. can usually be compared. The spectral distribution of the energy should also be comparable, especially at the intermediate to high κ end of the energy spectrum where turbulence is expected to be isotropic.

The performance of the numerical schemes for decaying turbulence is shown in Figs. 5–13, which cover Mach numbers M_1 values of 0.1, 0.5 and 0.7. These values represent increasing levels of the gradients of the flow variables. The flow fields computed by the ENO and compact differencing schemes are shown in the density contour map of Figs. 5 and 6 for $M_1 = 0.5$ and 0.7, respectively. Results are shown for a relative (to eddy turnover time) simulation time of 1.0. The compact and ENO results for $M_1 = 0.5$ are indistinguishable whereas those for $M_1 = 0.7$ show less satisfactory results for the compact schemes, as the representation of the density features are poor because of the presence of shocklets.
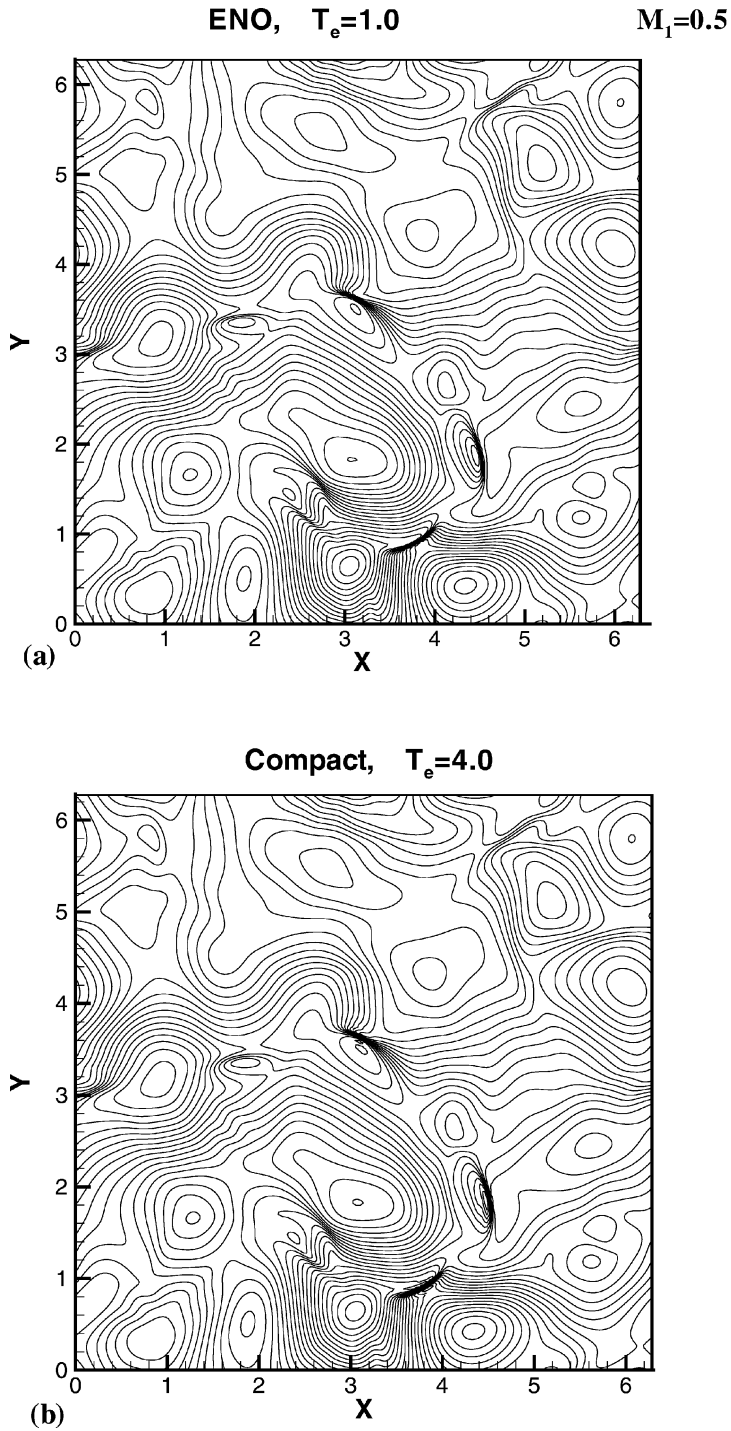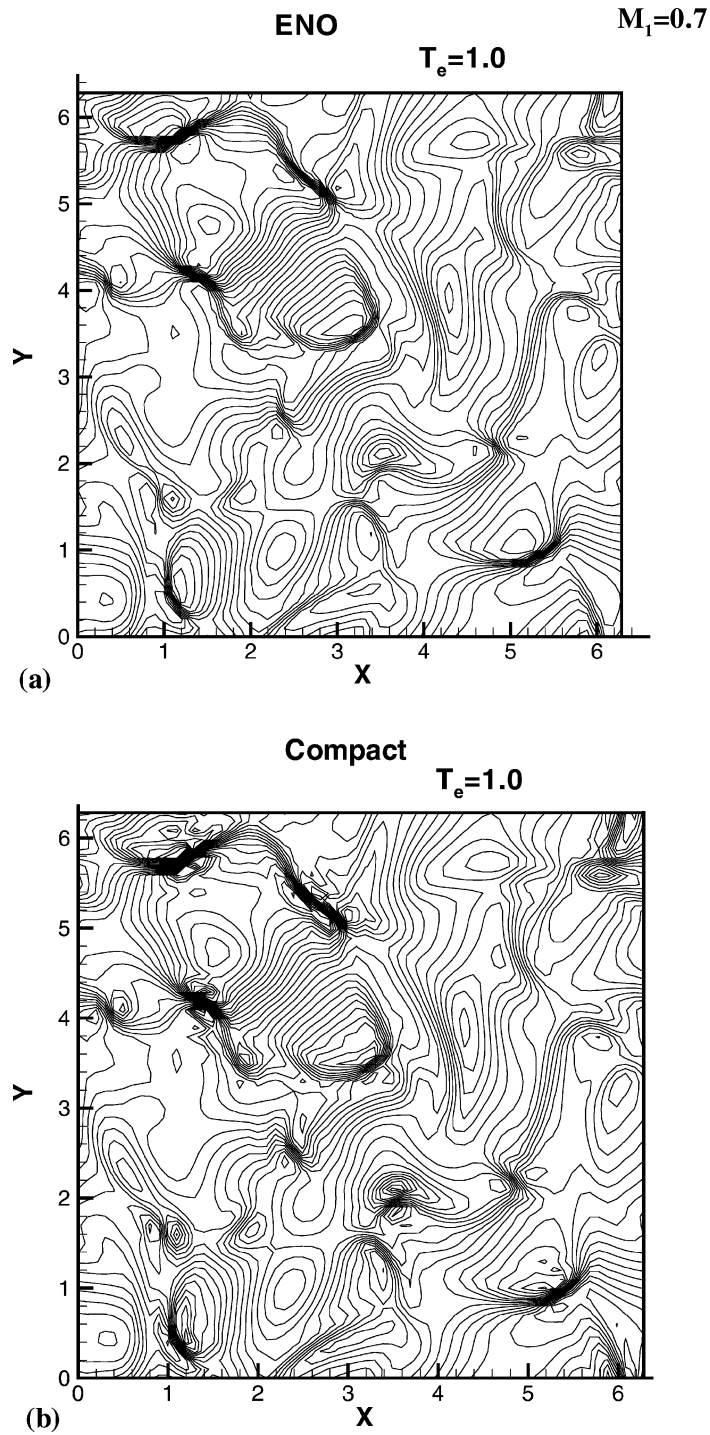
Fig. 5. The contour map of the density field at a simulation time (relative to the eddy turnover time) of 1.0. Results are provided for $M_1 = 0.5$; grid is 256^2. (a) *ENO* result. (b) *Compact scheme* result.

Fig. 6. The contour map of the density field at a simulation time (relative to the eddy turnover time) of 1.0. Results are provided for $M_1 = 0.7$; grid is 64^2. (a) *ENO* result. (b) *Compact scheme* results.

Nevertheless, this is an impressive performance by the compact code, in light of the fact that the features were not resolved. Of course, grid refinement (256^2, not shown) gave compact results that agree better with the ENO results.

Figs. 7 and 8 compare the performance of ENO, compact, pseudospectral, and a third-order, upwind-biased Roe scheme for the temporal evolution of the turbulence Mach number, $M_s^2(t)$, $E_k(t)$, and of $E_{int}(t)$, and the turbulence spectra for the kinetic and internal energy, $P_{kin}(\kappa)$, $P_{int}(\kappa)$, where κ is the wavenumber. The Mach number is $M_1 = 0.1$. The standard ENO scheme is used in Fig. 7 whereas in Fig. 8, fixed stencil ENO is used. For fixed stencil, $r \neq r(i)$, where r is the left shift in the stencil for cell i. Excellent agreement between compact and pseudospectral values is apparent. For ENO, because of the smooth field at this low Mach number, we see that the fixed stencil results agree better with the pseudospectral and compact results, whereas the adaptive stencil results are highly dissipative for M_s^2, E_k, and E_{int}. In all cases the low order Roe scheme gave unacceptably high dissipation.

With the exception of the low order Roe scheme, the agreement between the spectrum of $P_{kin}(\kappa)$ and $P_{int}(\kappa)$ is quite good at low κ values although the pseudospectral results for $\kappa = 2$ appear too high. In Fig. 7(c), the compact results have the correct energy dissipation at the large κ values. However, the energy for the ENO calculation does not decay beyond a certain κ value. This is attributable to fictitious turbulence energy generated by the adaptive stencil in ENO, as the fixed stencil results show a better dissipation phenomenon at large κ. It is interesting that this observation, which was first made by Rogerson and Meiburg [16] for an analytical (sine) function also applies to the Navier–Stokes equations for turbulence simulation. Perhaps more interesting is the fact the cure for the sine function [17] is also prescribable for the turbulence simulation case, in the manner just discussed. Note that the use of fixed stencil, while successful for $M_1 = 0.1$, is totally unacceptable for $M_1 = 0.5$ and $M_1 = 0.7$ because of the relatively large gradients. Specifically, the application of a fixed stencil for these Mach numbers, while giving very good results for $M_s^2(t)$, $E_k(t)$, and $E_{int}(t)$, totally destroyed the turbulence energy transfer process at large κ by generating unphysical $P_{kin}(\kappa)$ and $P_{int}(\kappa)$ values (not shown). For these higher Mach number cases, the adaptive ENO version gave spectra that compare more favorably with the compact and pseudospectral results. Even then, the spectra computed by the ENO method does not decay beyond a value of κ, as mentioned above (Fig. 9). Note in Fig. 9 that the WENO scheme does not have the difficulty of ENO in terms of energy decay at high wavenumbers. However, the WENO results are more dissipative, compared to ENO, compact, and pseudospectral.

In order to improve the energy decay characteristics of the ENO method at high wavenumbers, we added the VG filters to the standard ENO scheme, as discussed earlier in this paper. The results are shown in Fig. 10. The filter seems to have removed the effect of the adaptive grid in relation to the numerical turbulence at large κ. A more acceptable spectra decay behavior can now be observed. However, the filtered ENO results are less dissipative than the compact scheme, making the modified scheme potentially more useful for DNS or LES. It is important to note that both the ENO and compact scheme results shown in Fig. 10 use $\alpha_f = 0.4$.

For the compact scheme, the fidelity with which the spectra energy is dissipated at large κ can be adjusted with α_f (Fig. 11), with larger values resulting in decreasing dissipation. Note that α_f is bounded by $|\alpha_f| < 0.5$. In general, increasing filter order leads to a reduction in the amount of dissipation and hence the energy decay rate. A value of 0.499 in Fig. 11 gave results closer to those for the filtered ENO scheme using $\alpha_f = 0.4$ (not shown), suggesting that at high κ, filter is critical.

For the compact scheme, the effect of the order of differencing was investigated (Fig. 12) to better guide scheme selection for larger simulations where computational costs are large and the most efficient
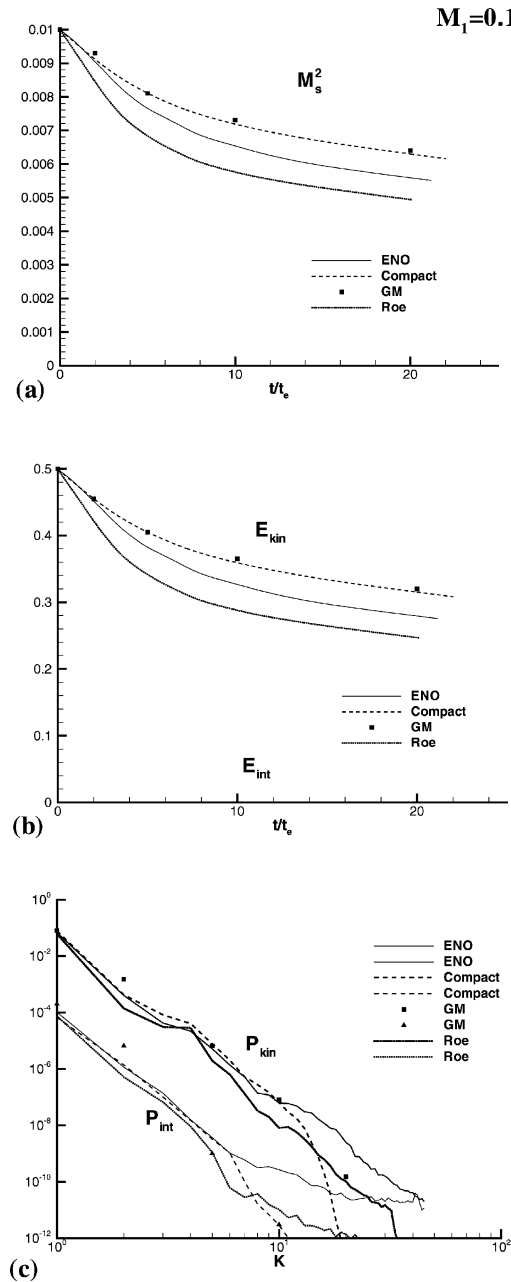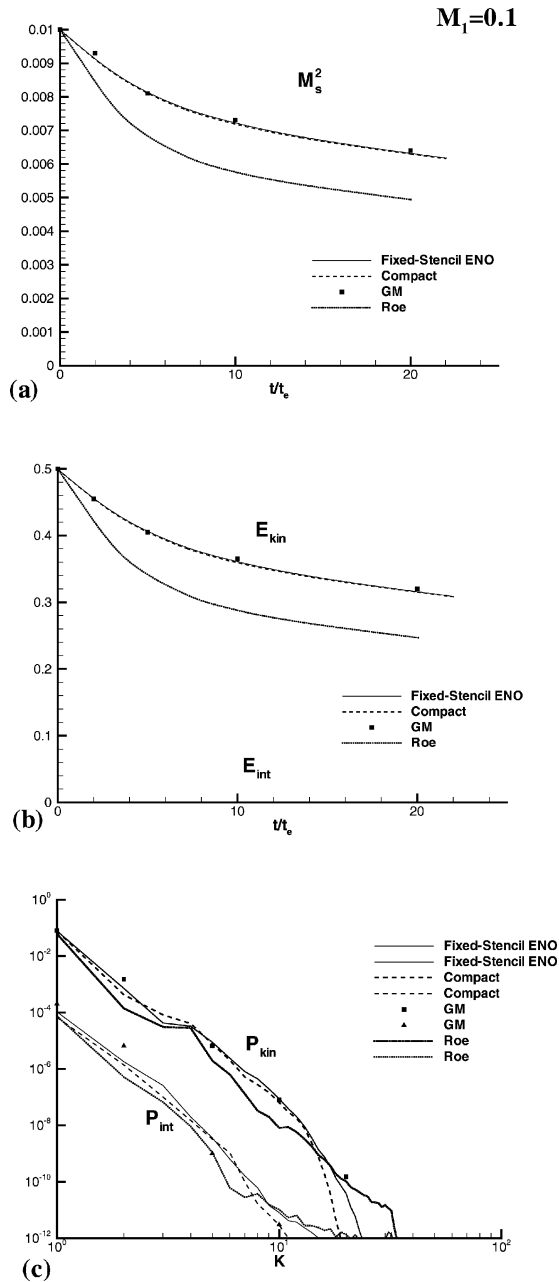
Fig. 7. Temporal variation of (a) the square of Mach number, and (b) the total kinetic and internal energy. (c) The spectral distribution of kinetic energy (P_{kin}) and internal energy (P_{int}). The x-axis in (a) and (b) is the simulation time relative to the eddy turnover time of turbulence. In (c) the x-axis is the wave number. The results are for Mach number $M_1 = 0.1$. In (a) and (b), filled square and triangular symbols are for the *pseudospectral* results, the dots are the *Roe* results, the dash lines are *compact scheme* results, whereas the solid lines are the *ENO* results. Note that the ENO results were obtained with an adaptive stencil. The results in (c) were taken at a relative simulation time of 20.

Fig. 8. Temporal variation of (a) the square of Mach number, and (b) the total kinetic and internal energy. (c) The spectral distribution of kinetic energy (P_{kin}) and internal energy (P_{int}). The x-axis in (a) and (b) is the simulation time relative to the eddy turnover time of turbulence. In (c) the x-axis is the wave number. The results are for Mach number $M_1 = 0.1$. In (a) and (b), filled square and triangular symbols are for the *pseudospectral* results, the dots are the *Roe* results, the dash lines are *compact scheme* results, whereas the solid lines are the *ENO* results. Note that the ENO results were obtained with a fixed stencil. The results in (c) were taken at a relative simulation time of 20.
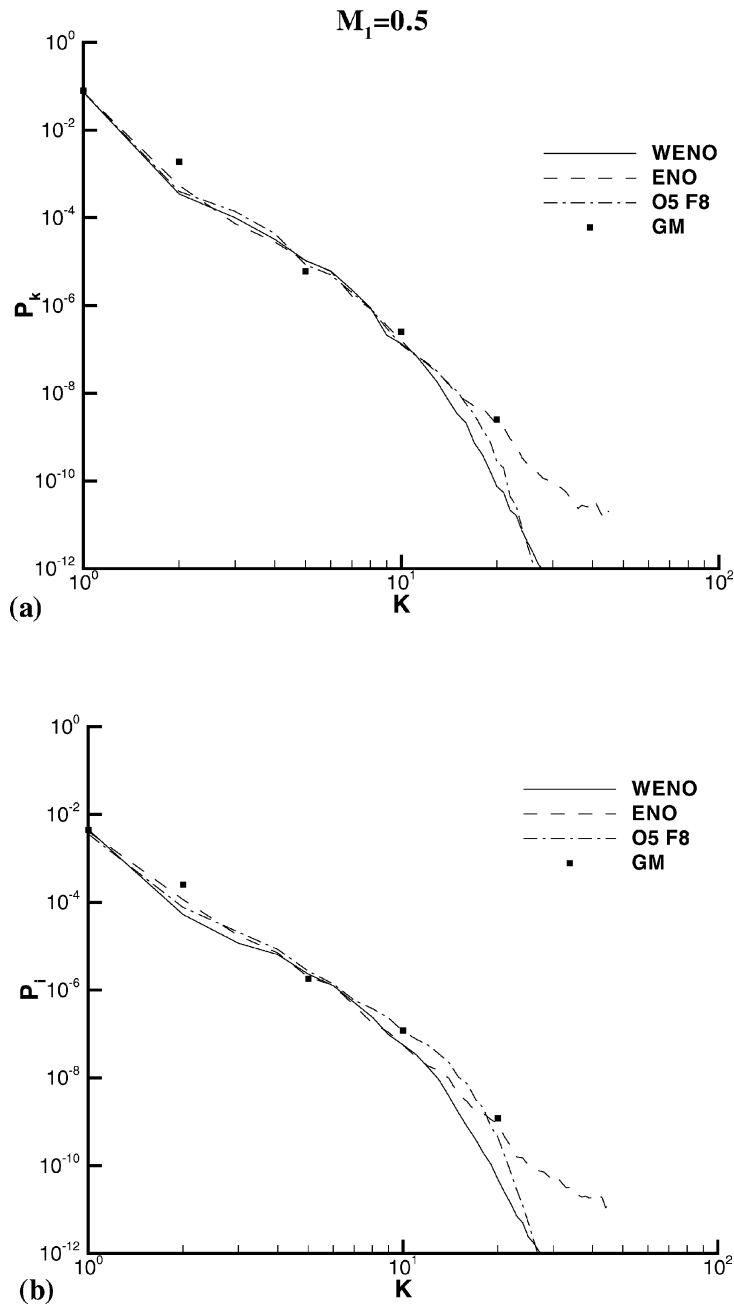
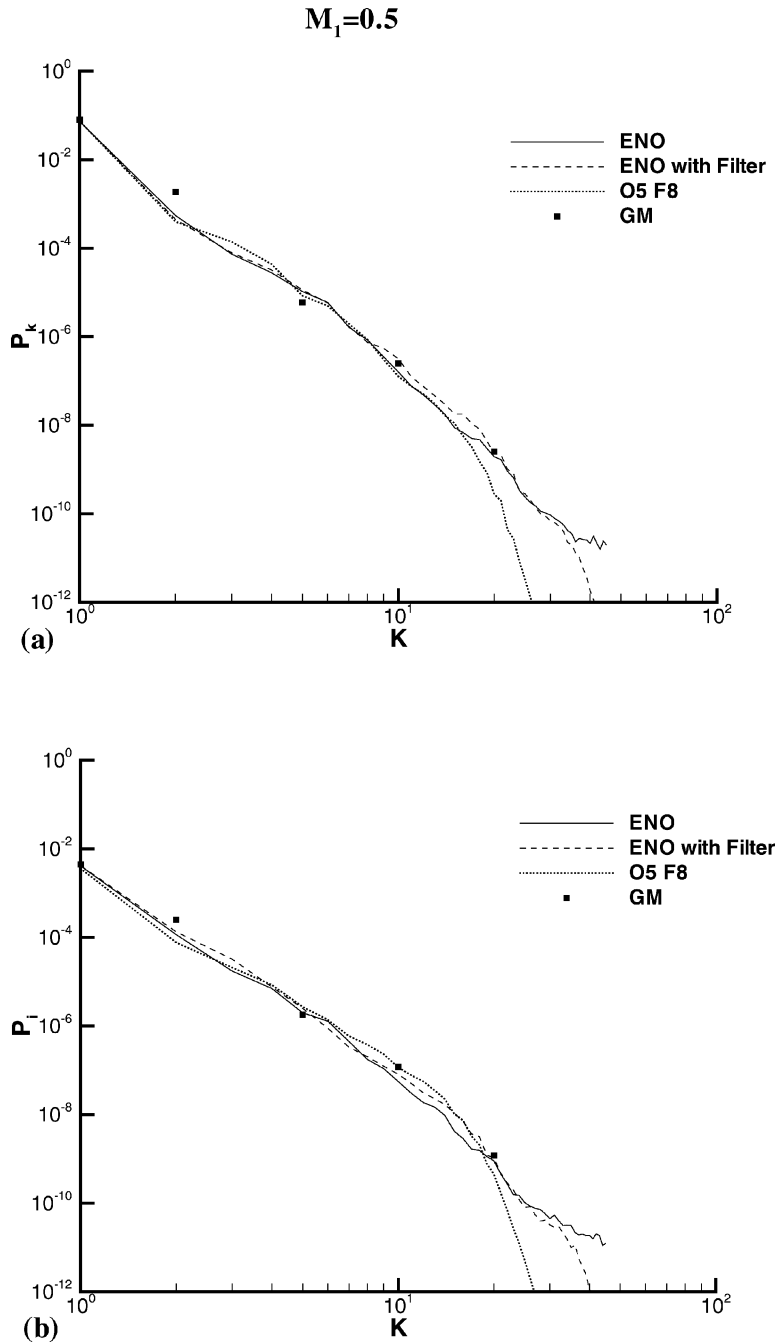Fig. 9. Comparative behavior of ENO, WENO, Compact, and pseudospectral schemes. Figure shows spectral distribution of kinetic energy of turbulence, P_{kin} (a), and internal energy P_{int} (b). The x-axis is the wavenumber. The results are for Mach number $M_1 = 0.5$ and the grid is 64^2. In these figures, filled square symbols (also referred to as GM in the figures) are for the *pseudospectral* results, the broken lines are filtered compact results (O5, F8, $\alpha = 0.4$), solid lines are WENO (unfiltered) and the dash lines are the ENO results. Note that the data were taken at a relative simulation time of 20.

Fig. 10. Spectral distribution of kinetic energy of turbulence, P_{kin} (a), and internal energy P_{int} (b). The x-axis is the wavenumber. The results are for Mach number $M_1 = 0.5$. In these figures, filled squares and triangular symbols are for the *pseudospectral* results, the dotted lines are filtered compact results (O5, F8, $\alpha = 0.4$), solid lines are unfiltered ENO results, while the dashed lines are the filtered ENO results (F8, $\alpha = 0.4$). Note that the data were taken at a relative simulation time of 20.
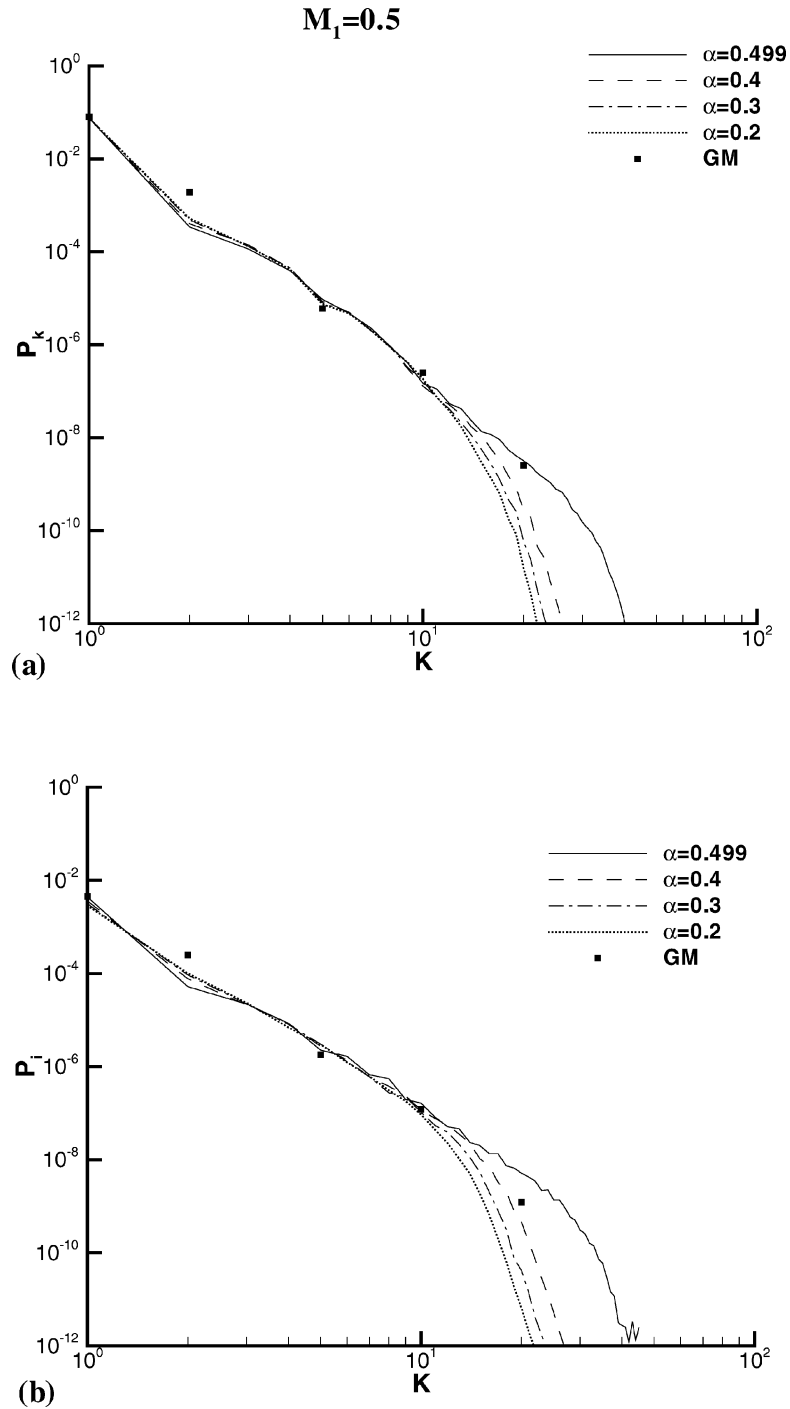
Fig. 11. Effect of filter coefficients (α) on the spectral turbulence energy distribution computed with the compact scheme. The results were taken at a simulation time (relative to the eddy turnover time) of 20.0 and for $M_1 = 0.5$. (a) The kinetic energy results. (b) The internal energy results.

Table 3
Relative CPU time consumption for direct simulation with 64^2 grid points on
DEC Alpha/2000

Number of time steps	10	10^2	2×10^2	10^3	1.5×10^3
ENO	1.633	1.572	1.653	1.600	1.588
Compact: with filter	1.0	1.0	1.0	1.0	1.0

schemes are required. The filter order was also varied. In the figure, O5 is an optimized fourth order scheme [6]. It is apparent that the order of compact differencing does not have any significant effect within the range studied, whereas the effect of filter order can be observed, consistent with the results in Fig. 11.

Grid convergence studies were undertaken to assess the quality of the results obtained with the 64^2 grid. Note that this grid was judged, using standard turbulence arguments, to be sufficient refinement necessary to resolve all scales of turbulence at the Reynolds number of 250 [7]. However, the results in Fig. 13 indicate that numerical convergence requirement is more restrictive than the turbulence resolution requirement, particularly for the compact scheme with $\alpha_f = 0.4$, the value used in Fig. 13. From previous discussions, larger α_f values produce more accurate results for the 64^2 calculations, bringing the results closer to that for 256^2. The agreement between the ENO results for 64^2 and 256^2 is quite good at intermediate wavenumbers, $5 \leqslant \kappa \leqslant 14$; the corresponding range for compact differencing is $5 \leqslant \kappa \leqslant 10$ at the value of α_f used for the computations in Fig. 13. Again, larger α_f values would extend this κ range. The main improvement of using 256^2 for ENO is in the removal of the numerical turbulence, thereby allowing the turbulence energy to decay continuously with κ without the use of the VG filters. Using the 256^2 results as the reference for comparison, it can be seen in Fig. 13 that the unfiltered ENO results (64^2) actually produce more accurate results than the filtered counterpart in $5 \leqslant \kappa \leqslant 14$, except that the former does not possess enough dissipation to remove the numerical turbulence at the tail end of the spectrum. The agreement between the compact and ENO results is much better at 256^2, although it should be recognized that the filter parameter can be adjusted in the compact differencing code, to serve as a means to substantially reduce the differences between the ENO and compact results.

Finally, the computational cost with the ENO and compact schemes is compared in Table 3, using the unoptimized versions of the two codes. It is pointed out that the values of the relative CPU times reported in this table are similar to those observed (not shown) for the simple functions discussed earlier in this paper. Therefore, for the various cases investigated, it is safe to say that the filtered compact code is approximately 1.5 times faster than the unfiltered ENO code.

7. Concluding remarks

High order schemes are required in numerical calculations intended for the direct and large eddy simulation of turbulence, where the physics must be accurately represented. The spectral method, which has traditionally been used for such calculations is not suitable when the Mach number becomes large. The reason is the nonlinear instability of the method, arising from the use of domain-global basis functions. Two promising candidates are compact and essentially nonoscillatory (ENO) schemes. Previous studies of these methods have not compared their relative ability to capture the spectral
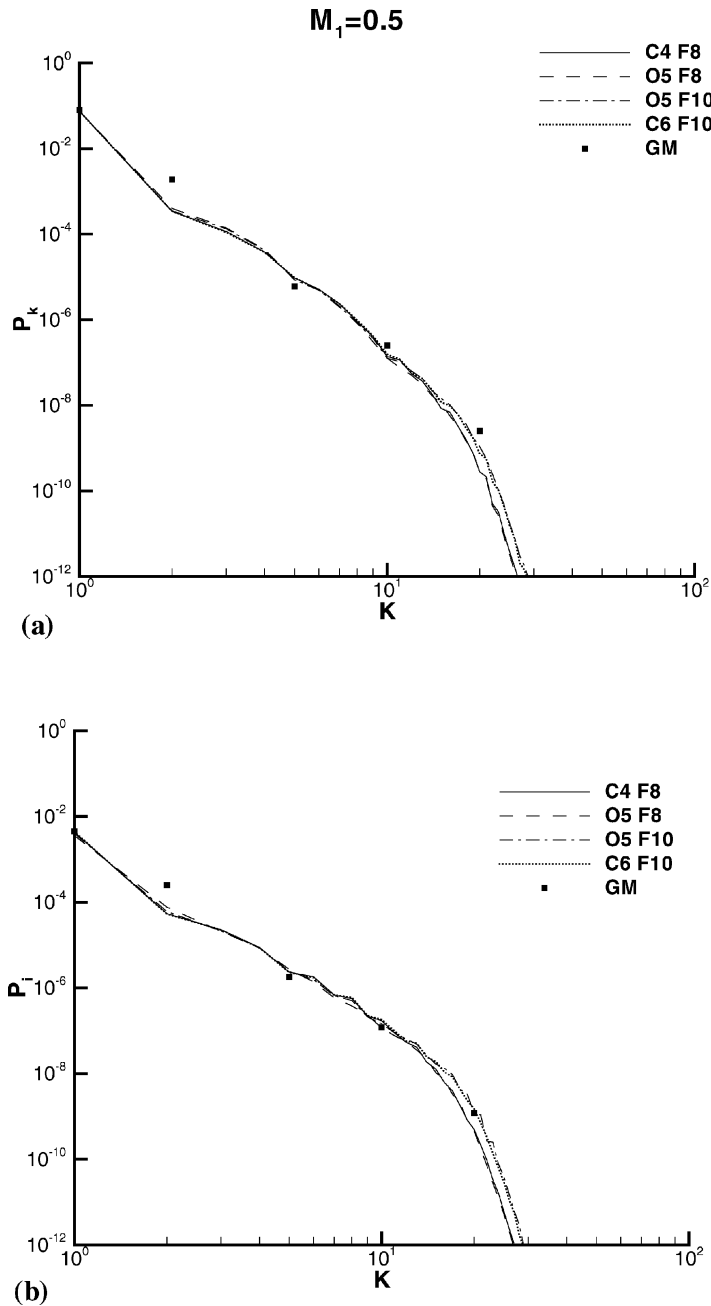
Fig. 12. Spectral distribution of kinetic energy, P_{kin} (a), and internal energy P_{int} (b). The x-axis is the wave number. The results are for Mach number $M_1 = 0.5$. In these figures, filled square and triangular symbols are for the *pseudospectral* results, the dots, dash, solid lines, etc., are *compact scheme* results where C4, F8 is 4th-order compact with 8th-order filter; O5, F8 is optimized 5th-order compact scheme with 8th-order filter; O5, F10 is optimized 5th-order compact with 10th-order filter, C6, F10 is 6th-order compact with 10th-order filter. Note that the data were taken at a relative simulation time of 20.
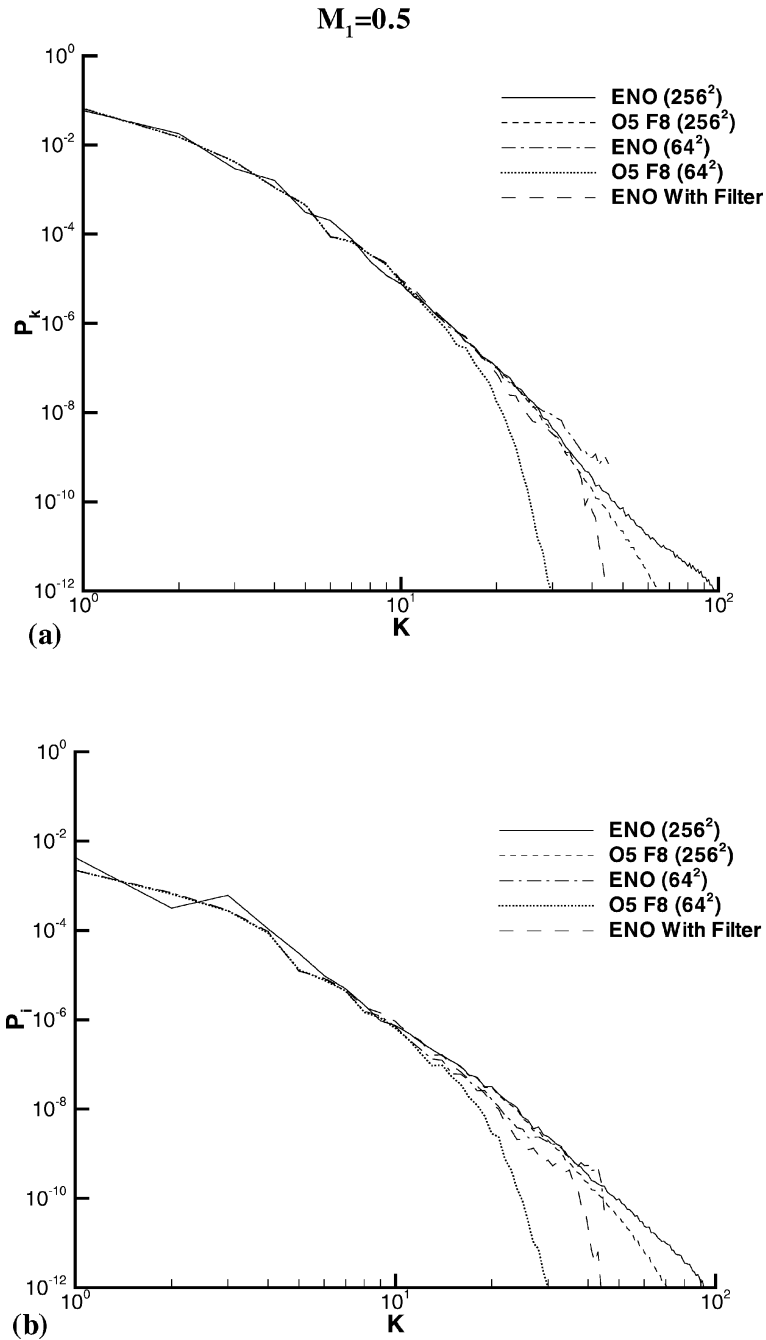
Fig. 13. The effect of grid refinement on the spectral distribution of kinetic energy of turbulence, P_{kin} (a), and internal energy P_{int} (b). The coarse grid is 642, the fine grid is 2562. The x-axis is the wavenumber. The results are for Mach number $M_1 = 0.5$. The compact results (O5, F8) used $\alpha = 0.499$, The filtered ENO results used $\alpha = 0.4$. Note that the fine grid compact and ENO results coincide at low wavenumbers. The data were taken at a relative simulation time of 4.0. No pseudospectral results are shown in this figure.

distribution of turbulence energy, which is a quantity of tremendous importance in theoretical turbulence and subgrid scale modeling in Large Eddy Simulation (LES).

The present study is significant in many respects. First, it focuses on the high wavenumber end of the turbulence spectrum and computes the relative performance of ENO, WENO, and compact differencing in that region. Second, to our knowledge, this study is the first to modify the standard ENO method to accept very high order filters (8th- and 10th-order accurate) and carry out numerical experimentation on them. A third significance of this work is the study of the spectral performance of WENO in a viscous Navier–Stokes application. Previous work on this relatively new scheme has focused mostly on the inviscid limit of the flow equations. Furthermore, even for the compact differencing case, which has been in use for almost a decade, the present study documents the effects of different filter orders on the fidelity of the method in representing the high wavenumber modes of turbulence. It has been observed in this work that the standard ENO scheme does not represent the tail end of the turbulence spectrum very well because of numerically-induced turbulence. However, the application of filters and, of course, grid refinement removes this difficulty. Finally, at low Mach numbers, the current compact differencing and filter scheme formulation gives better results but as the Mach number increases the relative suitability of the ENO method increases.

Acknowledgements

References

[1] X. Cai, E.E. O'Brien, F. Ladeinde, Uniform mean scalar gradient in grid turbulence: Asymptotic probability distribution of a passive scalar, Phys. Fluids 8 (9) (1996) 2555–2558.

[2] X. Cai, E.E. O'Brien, F. Ladeinde, Thermodynamic behavior in decaying, compressible turbulence with initially dominant temperature fluctuations, Phys. Fluids 9 (6) (1997) 1754–1763.

[3] X. Cai, F. Ladeinde, E.E. O'Brien, DNS on SP2 with MPI, in: C. Liu, Z. Liu (Eds.), Advances in DNS/LES, Greyden, Columbus, OH, 1997, pp. 491–495.

[4] D.J. Fyfe, Economical evaluation of Runge–Kutta formulae, Math. Comp. 20 (1966) 392–398.

[5] D. Gaitonde, J.S. Shang, Practical aspects of high-order accurate finite volume schemes for electromagnetics, Paper AIAA-97-0363, Reno, NV, 1997.

[6] D. Gaitonde, M.R. Visbal, High-order schemes for Navier–Stokes equations: Algorithm and implementation into FDL3DI, Technical Report # AFRL-VA-WP-TR-1998-3060, Air Force Research Laboratory, Wright-Patterson AFB, OH, 1998.

[7] S. Ghosh, W.H. Matthaeus, Low Mach number two-dimensional hydrodynamic turbulence: Energy budget and density fluctuations in a polytropic fluid, Phys. Fluids A 4 (1991) 148.

[8] A. Harten, S. Osher, B. Enquist, S. Chakravarthy, Some results on uniformly high order accurate essentially non-oscillatory schemes, Appl. Numer. Math. 2 (1986) 347–377.

[9] A. Harten, S. Osher, B. Enquist, S. Chakravarthy, Uniformly high order accurate essentially non-oscillatory, J. Comput. Phys. 71 (1987) 231–303.

[10] G. Jiang, C.-W. Shu, Efficient implementation of weighted ENO schemes, J. Comput. Phys. 126 (1996) 202–228.

[11] F. Ladeinde, E.E. O'Brien, X. Cai, An efficient parallelized ENO procedure for direct numerical simulation of turbulence, J. Sci. Comput. 38 (11) (1996) 215–242.

[12] F. Ladeinde, E.E. O'Brien, X. Cai, M. Liu, Advection by polytropic compressible turbulence, Phys. Fluids 48 (11) (1995) 2848–2857.

[13] S.K. Lele, Compact finite difference schemes with spectral-like resolution, J. Comput. Phys. 103 (1992) 16–42.

[14] X.-D. Liu, S. Osher, T. Chan, Weighted essentially nonoscillatory schemes, J. Comput. Phys. 115 (1994) 200–212.

[15] T. Passot, A. Pouquet, Numerical simulation of compressible homogeneous flows in the turbulence regime, J. Fluid Mech. 181 (1987) 441–466.

[16] A.M. Rogerson, E. Meiburg, A numerical study of the convergence properties of ENO schemes, J. Sci. Comput. 5 (2) (1990) 151–167.

[17] C.-W. Shu, Numerical experiments on the accuracy of ENO and modified ENO schemes, J. Sci. Comput. 5 (2) (1990) 127–149.

[18] C.-W. Shu, Essentially non-oscillatory and weighted essentially non-oscillatory schemes for hyperbolic conservation laws, ICASE Report No. 97-65, 1997.

[19] C.-W. Shu, S. Osher, The efficient implementation of essentially non-oscillatory shock-capturing schemes, J. Comput. Phys. 77 (1988) 439–471.

[20] C.-W. Shu, S. Osher, The efficient implementation of essentially non-oscillatory shock-capturing schemes, II, J. Comput. Phys. 83 (1989) 32–78.

[21] C.-W. Shu, T.A. Zang, G. Erlebacher, D. Whitaker, S. Osher, High order ENO schemes applied to two- and three-dimensional compressible flow, Appl. Numer. Math. 9 (1992) 45–71.

[22] J.F. Thompson, Z.U.A. Warsi, C.W. Mastin, Numerical Grid Generation, North-Holland, New York, 1985.

[23] M.R. Visbal, D.V. Gaitonde, High-order accurate methods for unsteady vortical flows on curvilinear meshes, Paper AIAA-98-0131, Reno, NV, 1998.